Heterogeneous Dual-Source Fuel-Cell Powertrain for Battery-Free Electric Aircraft: A Feasibility Simulation Study

Mehdi Seddiq

***Abstract*—Hydrogen fuel-cell propulsion for regional aircraft is presently constrained by transient performance that falls short of what the application requires, at both stack and system level. This is commonly addressed by adding a battery or supercapacitor to absorb rapid load changes, though the additional mass and volume reduce the attractiveness of fuel-cell propulsion. This paper proposes an alternative: to employ two fuel-cell sources, one mainly for steady-state operation and a second specialised for transient loads, so that the powertrain follows load changes without additional stored energy. Such heterogeneity between sources does not appear to have been examined as a means of meeting flight transients. A simulation study is reported, comparing this dual-source powertrain against a single-source configuration sized to deliver the same aggregate nominal exchange current, neither of which uses a battery or other storage device. For a commanded load rise, the dual-source configuration reduces peak current in the primary fuel-cell source by 36% and requires 29% less total membrane area, while delivering 7.5% more peak propeller power at 7.0% higher mean efficiency. Peak current density in the primary source is unchanged; the relief is therefore not obtained by operating any part of the system harder. The auxiliary fuel-cell source sustains a rate of change of current density approximately 5.7 times that of the primary source, and leads it in phase, indicating a division of labour in timing as well as in magnitude. The advantage persists across repeated load events. These results are obtained from a single load profile, with parameters that are calibrated, not independently validated. They establish a precondition for flight capability, not a demonstration of it. Nevertheless, they indicate that heterogeneous parallel fuel-cell sources merit further investigation as a route to battery-free fuel-cell aircraft.**

***Index Terms*—Battery-free propulsion, electric aircraft propulsion, multi-stack fuel cell systems, power management, proton exchange membrane fuel cells, transient response.**

I. Introduction

Aviation is under sustained pressure to decarbonise, and hydrogen-electric propulsion has moved from concept studies into industrial development programmes. Airbus and MTU Aero Engines announced in July 2026 their intention to establish a joint venture dedicated to the development and commercialisation of a fully electric hydrogen fuel-cell engine [1], while ZeroAvia is developing hydrogen-electric powertrains spanning the 10–20 seat class [2] and 40–80 seat regional turboprop class [3]. These programmes share a common architecture, in which a proton-exchange membrane (PEM) fuel-cell system supplies electrical power to one or more propulsion motors. They also share a common difficulty; fuel cells deliver high specific energy but respond slowly to rapid changes in load, and the flight phases that matter most for certification, namely take-off, initial climb, go-around and engine-out operation, are precisely those in which power demand rises quickly. Where a battery is present to absorb these transients, the limitation remains largely hidden. Where the battery is removed, it becomes the constraint that governs the design.

The conventional response is hybridisation. Pairing a fuel cell with a battery or supercapacitor allows the fuel cell to supply the slowly varying bulk of the mission energy while the storage element absorbs fast demand [4], [5]. This arrangement is well understood, and energy-management strategies for it are the subject of an extensive literature [6], [7]. However, this comes with increased mass as its cost. Batteries with the power density required for take-off and climb have comparatively low energy density, so the storage element contributes weight throughout a mission in which it is heavily used only briefly [8], [9]. In aviation this penalty compounds, because additional mass increases the power required in every phase of flight, which in turn increases the size of the propulsion system that must carry it [10]. The question that follows is whether the fuel-cell system can be made to absorb these transients itself, allowing the storage element to be minimised or removed altogether. This question is being pursued industrially as well as academically: a recent NASA trade-space study for fuel-cell-powered aircraft includes an explicitly battery-free configuration among the architectures assessed [11], and a battery-free aircraft fuel-cell system has been patented [12].

The transient limitations of PEM fuel cells are well characterised at cell level. Following a step increase in current, the terminal voltage falls and recovers over a period governed by several coupled processes: oxygen depletion in the cathode catalyst layer and gas-diffusion medium, which drives the cell into concentration polarisation [13], [14]; the response of the air-path compressor, which cannot raise cathode stoichiometry instantaneously [15]; and slower changes in membrane hydration and stack temperature, the latter being of particular significance under the ambient conditions encountered in flight [16]. The design levers acting on these processes are equally well studied, and include membrane thickness [17], flow-field geometry [14], cathode catalyst layer composition [18], and control of stoichiometry and operating pressure [19], [20]. This body of work establishes that a cell can be configured for fast

M. Seddiq is with the School of Science and Technology, City St George's, University of London, London EC1V 0HB, U.K. (e-mail: mehdi.seddiq.4@city.ac.uk). Correspondence may also be sent to mehdiseddiq@gmail.com.

response, and that doing so generally costs efficiency at steady operation. The present study treats these cell-level characteristics as boundary conditions, not as objects of investigation, and adopts representative parameter sets accordingly.

Distributing load across multiple fuel-cell stacks is an established alternative to increasing the capability of a single one. Multi-stack architectures have attracted attention because they allow power demand to be shared, relieving localised thermal and electrical stress, improving part-load efficiency through selective stack activation, and providing redundancy against the failure of any one stack [21], [7]. Because individual stacks cannot follow load changes as quickly as the load imposes them, multi-stack studies have generally addressed the transient problem through the power-electronic interface, using active current-sharing control between converters to allocate demand dynamically [22], [6]. What these studies share is an assumption that receives little scrutiny: the stacks are nominally identical, and are differentiated only by their operating point and by the scheduling logic applied to them. Heterogeneity between stacks has been examined in one respect. Ngo and Kim propose an asymmetric multi-stack system of differently rated stacks for a fuel-cell electric bus, distributing power so that each operates near its efficiency optimum [23], and Eom *et al.* compare a dual-stack automotive powertrain against a single-stack equivalent [24]. Both retain a battery, which absorbs the fast component of the drive cycle, and in both the heterogeneity serves steady-state efficiency rather than transient capability. Design heterogeneity between stacks, in which one is configured for fast response and another for efficient steady operation, has not been examined as a means of meeting mission transients without a storage element.

II. System Architecture and Simulation Model

A. Powertrain Topology

The paper compares two configurations. The dual-source architecture, denoted D, comprises two fuel-cell sources, FC1 and FC2. The single-source comparator, denoted S, uses FC1 alone, sized to equivalent capability according to the criteria in Section III. Both configurations share the same topology: two branches, each pairing a fuel-cell source with its own DC-DC converter, feed a shared DC bus through a diode-OR connection, which in turn supplies a three-phase inverter driving a permanent-magnet synchronous motor and fixed-pitch propeller. In S, FC2 remains physically present but carries no load, preserving structural symmetry with D. No battery, supercapacitor, or other electrical energy-storage device is used in either configuration. Fig. 1 shows the complete topology; component-level circuit parameters are provided in the supplementary material. The converters are represented by behavioural models that regulate output voltage without simulating individual switching events, and the inverter by an average-value voltage-source converter. In such a system, the dynamics reported arise from the electrochemical, electrical and mechanical time constants of the system.

B. Role-Specialised Fuel-Cell Sources

FC1 and FC2 are differentiated by active area, cell count and dynamic response, following the bulk-energy and fast-transient roles introduced above. Table I lists the parameters used for both. FC1's parameters follow a conventional PEM stack configuration of the kind characterised in [17], [15], while FC2's parameters represent a high-performance but physically plausible design optimised for fast response, not necessarily a widely commercialised product [18], [19]. Both are calibrated toward physically plausible polarisation and transient behaviour from these starting points, consistent with the empirical-tuning limitation noted in Section V-E.

TABLE I
Fuel-Cell Source Parameters

Parameter	FC1	FC2
Open-circuit voltage per cell (V)	1.0	1.0
Cells in series	650 (65×10)	390 (26×15)
Active area per cell (cm^2)	300	50
Parallel strings, D	7	8
Parallel strings, S	11	inactive
Tafel slope (V)	0.0304	0.0195
Internal resistance (Ω)	0.003064	0.00225
Nominal exchange current (A)	4.2	2.4
Collapse current (A)	2100	700
Electrical time constant (ms)	20	5

At this sizing, D's total fuel-cell active area is 152.1 m^2 (FC1: 136.5 m^2; FC2: 15.6 m^2), against 214.5 m^2 for S's FC1 alone: 29% less fuel-cell material at equal comparator sizing. This reduction is specific to the fuel-cell stacks and does not extend to converter or bus-component sizing, which are not compared on this basis.

C. Converter Interface and Bus Coupling

Each converter's output is diode-OR connected onto the shared bus, so an independently set voltage reference on one converter can reverse-bias its diode and disconnect that branch from the bus without warning; Section II-D describes how the supervisor avoids this. The two converters additionally differ in output-voltage droop, a standard current-sharing mechanism for parallel-connected sources [25].

D. Supervisory Power Management

Power sharing is governed by a transparent, rule-based supervisory scheme of the kind widely adopted in multi-stack systems for its low computational cost and predictability [7], [26]; no optimisation-based control is applied in either configuration, so the architectural comparison is not confounded by controller sophistication. A rate limiter tracks the commanded throttle to a real-time power target, and a bounded, additive look-ahead term anticipates rises within a fixed 0.5 s horizon, avoiding the saturation an unbounded multiplicative boost would produce over a fast ramp. A three-state hysteretic switch, steady, transition and transient, blends FC1 and FC2 power-sharing coefficients according to the anticipated rate of power change, with separate entry and exit thresholds preventing chattering. The supervisor also computes a bounded offset between the two converters' voltage references, anchoring Converter 2's target to Converter 1's, which prevents the reverse-bias disconnection described in Section II-C and governs how transient current is shared between the branches.

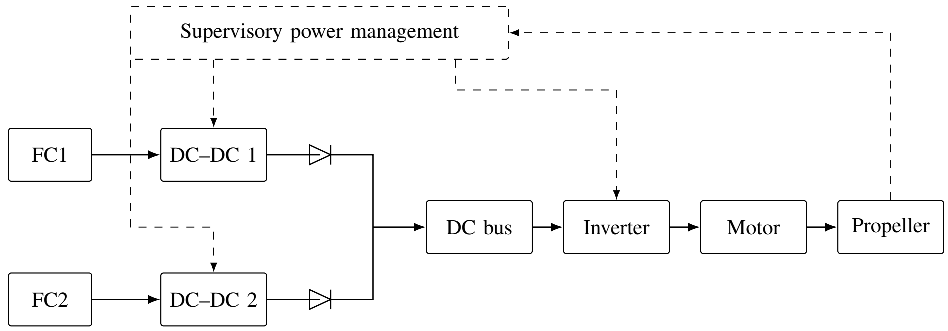

Fig. 1. Powertrain topology in single-line form. Each fuel-cell source feeds its own DC–DC converter, and the two converter outputs are diode-OR connected onto a shared DC bus supplying the inverter, permanent-magnet synchronous motor and fixed-pitch propeller. Each branch additionally contains a resistor, inductor and RC snubber, omitted here for clarity. Dashed lines denote control signals. No battery, supercapacitor or other electrical energy-storage device is present.

S retains the same rate limiter and look-ahead structure, with FC1 alone carrying the full demand, keeping control sophistication equal between the two arms. Since each branch's converter, geometry and coefficient schedule can be specified independently, this transparent baseline leaves considerable scope for further improvement, a point Section VI returns to.

E. Load Profile and Simulated Conditions

The load profile holds a baseline throttle for a settling period, then commands a linear rise to a fixed peak throttle over a 0.375 s ramp, sustained thereafter. The ramp is not shortened further because a faster rise drives FC2 to its collapse current in D. Raising this bound, by resizing FC2 or by limiting its share of the transient, is left to future work. This single-rise profile is the case reported here; the two-cycle variant used in Section IV-E to test repeatability commands two raised-cosine rises separated by a stabilisation period. For every run, statistics and figures are computed from the true transient onset, excluding a brief solver-initialisation transient, to the end of the recorded window.

III. Comparability Framework

Comparing D against S requires the single-source system to be sized on a defensible basis. This is not a neutral step. A sizing basis that appears reasonable as a functional criterion may still entail a considerable difference between the architectures in the amount of active material used. As a result, an observed difference in behaviour can reflect the sizing choice rather than the architecture under test. In the multi-stack literature the basis is generally asserted and its influence on the reported outcome is seldom examined [6], [7], [27].

A. Equivalence Criteria

Table II lists the criteria considered. Each defines equivalent capability differently, and each is defensible in isolation; they do not, however, yield the same comparator. Sizing S by equal total active area, equal collapse current and equal aggregate nominal exchange current gives $N_{p,\mathrm{S}} = 7.8$, 9.3 and 11.0 respectively, a spread wide enough that the comparison may be sensitive to the criterion adopted. Only the third is simulated here; quantifying that sensitivity by running the comparator at each sizing is left to future work.

TABLE II
Equivalence Criteria for Sizing the Single-Source Comparator

Criterion	Principal limitation
Equal rated capacity	Says nothing about transient capability
Equal total active area	Favours the arm with faster electrochemistry
Equal aggregate exchange current	Ties equivalence to a single calibrated parameter
Equal collapse current	Rests on a conservative design threshold, not a validated limit
Equal current density at design point	Requires a design point to be fixed in advance
Uniform high-performance material	Assumes an untested manufacturing premise
Equal mass	Requires balance-of-plant data not modelled here
Equal volume	As above
Equal material cost	Not actionable; cost data unavailable

Matching parallel-string count is excluded as a criterion, since FC1 and FC2 differ in area per cell and equal string counts therefore correspond to unequal active area.

B. Performance Metrics

Once both configurations are sized, they are compared on quantities normalised so that sources of different physical size can be compared on a common basis. Current is expressed as current density, J (A/cm^2), and its rate as dJ/dt (A/cm^2·s), both normalised by the current-carrying area $N_p \times A_{\mathrm{cell}}$. Voltage is expressed as the fraction V/OCV and its rate as dV/dt in OCV/s. The comparison also uses overall energy efficiency, propeller mechanical power and its rate, and the integral of each rate quantity over the analysis window as a cumulative stress measure.

C. Meta-Criteria and Criterion Selection

Since no single equivalence criterion is uniquely correct, the criteria themselves are judged against a further set of considerations: physical interpretability; robustness to uncertainty in the underlying calibrated parameters; isolation, meaning how cleanly the criterion separates the architectural effect under test from confounding factors; manufacturability; communicability; and relevance to the research question. A full statement of every criterion and metric against these considerations is provided in the supplementary material.

Based on this, S is sized by equal aggregate nominal exchange current, giving $N_{p,\mathrm{S}} = 11$. This criterion was preferred as it refers to an intrinsic electrochemical property of the sources being compared, remains meaningful whichever operating point the transient reaches, and reflects charge-transfer kinetics directly relevant to a comparison centred on transient response. Its principal limitation is that nominal exchange current is itself among the parameters empirically tuned for this model; the sizing basis therefore inherits the calibration uncertainty already noted for the source parameters in Section II, and does not introduce a further, independent source of uncertainty. The criterion also does not directly target transient tolerance, the property under investigation: equal exchange current does not by itself guarantee equal capability to withstand a given rate of load change, and establishing that connection quantitatively is left to future work.

D. Material Consequences of the Sizing Basis

No criterion in Table II is neutral with respect to installed material. Referred to D's total active area of 152.1 m^2, sizing S by equal collapse current, a criterion not used to size any run reported in this paper, would require 182.0 m^2, some 20% more, while the adopted exchange-current basis requires 214.5 m^2, some 41% more.

Two consequences follow. First, a criterion's material implications are not visible from its own statement; they emerge only once the resulting configurations are constructed and their material budgets compared. Second, the comparator used throughout this paper is the more generously sized of the practical options: any transient advantage reported for D in Section IV is therefore measured against a single-source system built with 41% more active area.

IV. Results

This section reports the response of the two configurations to a commanded load rise. Unless stated otherwise, all quantities are evaluated over an interval of 5.0 s beginning at the transient onset defined in Section II, which extends well beyond the point at which propeller power has settled. Time is measured from that onset throughout, so that the commanded rise begins at $t = 0$ and the interval before it appears at negative time.

A. System-Level Response

Fig. 2 shows the commanded throttle alongside propeller power, fuel-cell electrical power and overall efficiency for both configurations. Propeller power rises from its baseline value to 179.1 kW in D and 166.6 kW in S within about 0.3 s, shortly before the command reaches its peak at 0.375 s, and declines slowly thereafter. Mean overall efficiency over the evaluation interval is 0.746 for D and 0.697 for S, a relative improvement of 7.0%.

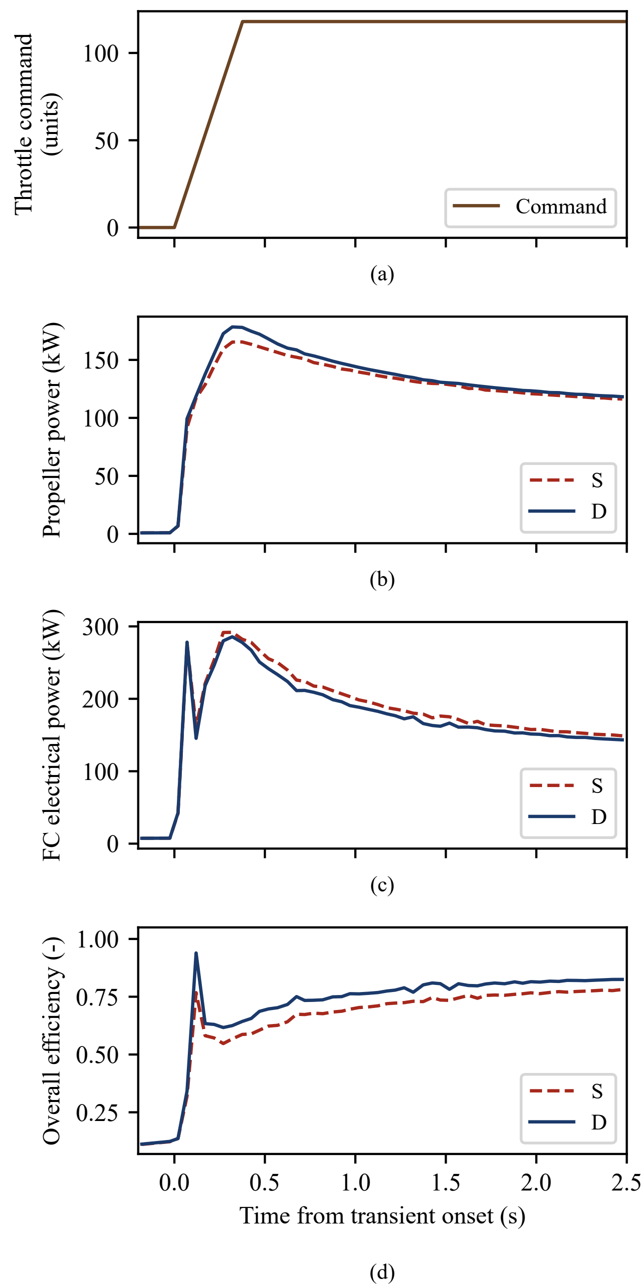

Fig. 2. System-level response to the commanded load rise, shown at 0.05 s bin resolution. Time is measured from the transient onset. (a) Commanded throttle. (b) Propeller power. (c) Fuel-cell electrical power. (d) Overall efficiency.

D delivers this higher propeller power while drawing less from the sources: rms fuel-cell electrical power is 165.3 kW in D against 172.2 kW in S, a reduction of 4.0%, and Fig. 2(c) shows S above D throughout the decay. The current within that lower total is also distributed differently. Peak FC1 current is 395.1 A in D against 621.1 A in S, a reduction of 36.4%, and the rms value is 213.9 A against 316.6 A, a reduction of 32.4%; the balance in D is carried by FC2, which reaches a peak of 408.3 A. Peak FC1 current density is unchanged between the configurations at 0.188 A/cm^2, so the relief afforded to FC1 is not obtained by operating it at

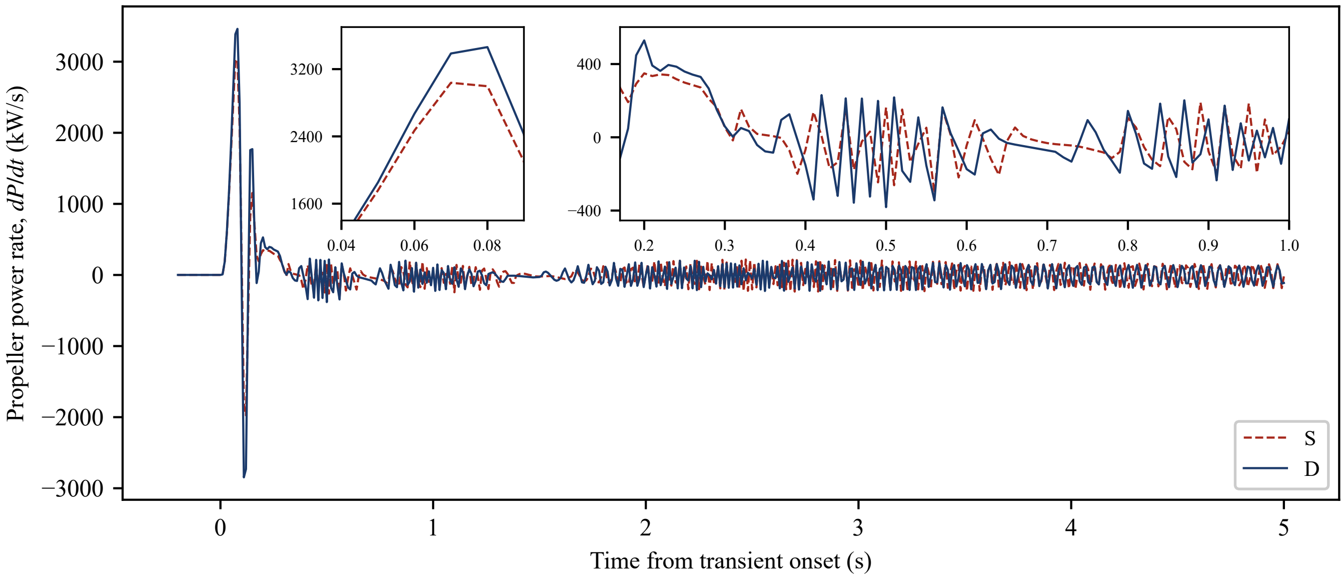

Fig. 3. Rate of change of propeller power over the full evaluation interval. The first inset resolves the initial peak; the second resolves the settled region following the transient.

a higher intensity per unit of active area. Section IV-D sets the two sources' duties alongside the membrane area each configuration requires.

Fig. 2(c) also shows a sharp rise and fall in fuel-cell electrical power over the first 0.12 s, present in both configurations. This is not attributable to the branch snubbers, whose time constant of 50 μs is some three orders of magnitude shorter than the feature. Over the same interval the propeller accelerates by about half, from 220 to 329 r/min, while both fuel-cell currents fall by more than 80% and the bus voltages change by under 1%. The most plausible explanation is therefore the motor back-electromotive force, which is small while the machine is still slow and rises quickly as it accelerates, reducing the current the inverter draws. The present model was not constructed to separate this from other contributions, and the attribution should be read as indicative.

B. Rate of Change of Delivered Power

Fig. 3 shows the rate of change of propeller power on the same onset-relative time axis, presented at full sampling resolution rather than bin-averaged, since the overshoot and undershoot structure at the onset of the transient is lost under averaging.

D achieves a peak rate of change of propeller mechanical power of 3462 kW/s against 3038 kW/s for S, an increase of 14.0%, and a corresponding peak rate of change of fuel-cell electrical power of 8484 kW/s against 7703 kW/s, an increase of 10.1%. D therefore both accelerates the propeller more rapidly and admits a faster excursion in electrical power, while imposing the lower FC1 current reported in Section IV-A.

The oscillation that follows the transient persists to the end of the interval without decaying, and is of comparable amplitude in both configurations. Its dominant frequency is 29.0 Hz in S and 27.6 Hz in D; these values were obtained from the sampled data, as the figure does not resolve individual cycles at this scale. A linear regression of the rate of change of fuel-cell electrical power against the rate of change of propeller power gives a correlation coefficient of 0.607 for S and 0.617 for D, a measure returned to in Section V-B.

C. Trajectory of the Transient

Fig. 4 presents the same transient as a trajectory in the plane formed by power and its rate of change, for fuel-cell electrical power and for propeller power. This representation removes time as an explicit variable and shows the path each configuration follows between its initial and final states.

Both configurations trace closed trajectories. D encloses the larger trajectory in both planes, its negative excursion in fuel-cell power rate reaching $-10\,414$ kW/s against -7176 kW/s for S. The enclosed area measures the phase displacement between a quantity and its own rate of change, so a larger area indicates a response departing further from a purely proportional relationship between power and its rate.

D. Division of Labour Between the Sources

Fig. 5 shows the current-density rate of each source against the rate of change of fuel-cell electrical power. Panel (a) compares FC1 in S and in D; panel (b) adds FC2.

A linear regression of FC2's current-density rate against FC1's gives a slope of 5.70 with a correlation coefficient of 0.935. For a given excursion in system power, FC2 therefore sustains a rate of change of current density approximately 5.7 times that of FC1.

Table III sets the consequence for FC1 alongside the material required to obtain it. Peak FC1 current falls by 36.4% between the configurations, and accumulated current and current rate over the transient fall by 32.2% and 40.0% respectively, while peak FC1 current density is unchanged.

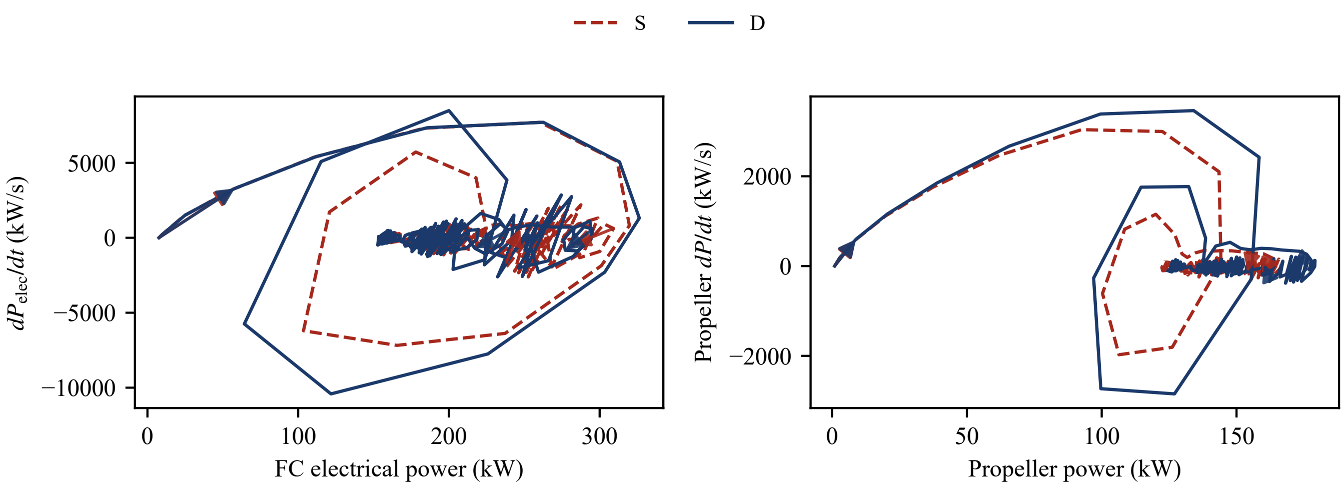

(a) (b)

Fig. 4. Trajectories of the transient in the power–power-rate plane. (a) Fuel-cell electrical power. (b) Propeller power. Arrows indicate the direction of traversal.

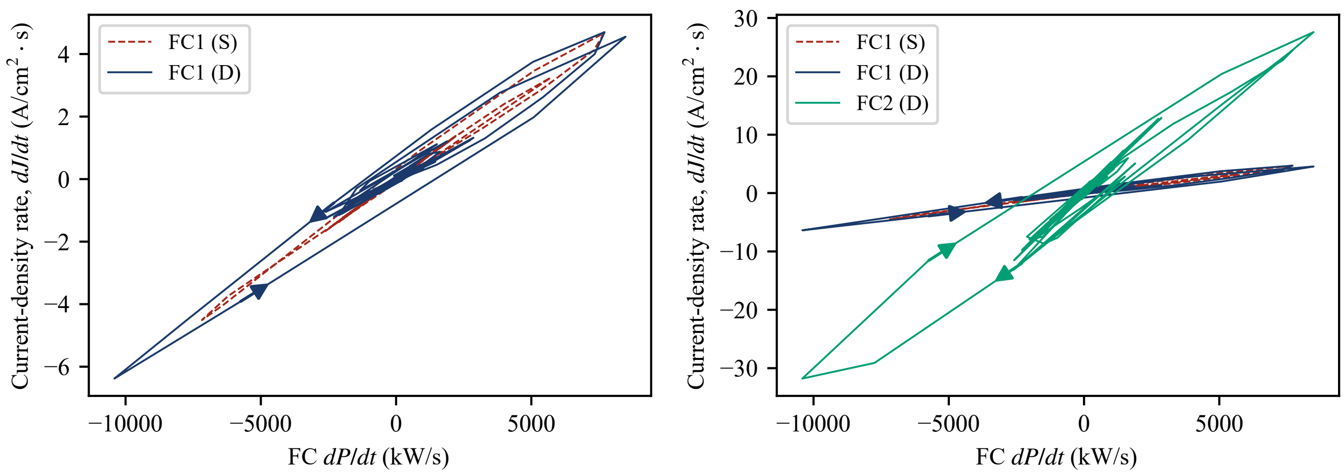

(a) (b)

Fig. 5. Current-density rate against fuel-cell electrical power rate. (a) FC1 in both S and D. (b) All three sources, with FC2 of the dual-source configuration included. Note that the vertical scales of the two panels are different, that of panel (b) spanning approximately six times the range of panel (a). Arrows indicate the direction of traversal.

TABLE III
ELECTROCHEMICAL DUTY AND ACTIVE AREA

Quantity	S	D	Change
FC1 peak current (A)	621.1	395.1	−36.4%
FC1 accumulated current (A·s)	1517.4	1029.3	−32.2%
FC1 accumulated current rate (A)	3080	1847	−40.0%
FC1 peak current density (A/cm^2)	0.188	0.188	0.0%
Total fuel-cell active area (m^2)	214.5	152.1	−29.1%

Note that this relief is obtained with less material: total fuel-cell active area falls from 214.5 m^2 in S to 152.1 m^2 in D, a reduction of 29%, and D simultaneously delivers the higher propeller power and draws the lower fuel-cell electrical power reported in Section IV-A.

The peak current density reached by FC2 is 1.02 A/cm^2, against 0.188 A/cm^2 for FC1. The two sources therefore operate on opposite sides of the peak-power point of the polarisation curve, which for PEM cells falls at approximately 0.6–1.2 A/cm^2 depending on technology level [28]. FC1 operates well below this point, in the high-voltage region where cell efficiency is greatest, while FC2 operates close to it, where power density is greatest and stack mass is least. Neither approaches the limiting current, typically 1–2 A/cm^2. The difference between the two follows from the heterogeneous sizing and not from any difference in the electrical conditions imposed on them.

The direction in which each trajectory in Fig. 5 is traversed is determined from the signed area it encloses, computed on the time-ordered samples with both axes normalised by their standard deviations. A positive area corresponds to anticlockwise traversal and a negative area to clockwise traversal; for two signals of relative phase φ, the enclosed area is proportional to $-\sin\varphi$, and its sign therefore indicates whether the vertical quantity leads or lags the horizontal one. The two FC1 trajectories are traversed anticlockwise and the FC2 trajectory clockwise, so that FC1's current-density rate lags the fuel-cell power rate in both S and D, whereas FC2's leads it. A cross-correlation of the two signals gives the same ordering, though the phase differences are smaller than the 10 ms sampling interval and were resolved by interpolation.

This difference in sign follows from the supervisory scheme of Section II-D. FC1's allocation is governed by the power presently delivered, whereas the variable part of FC2's is governed by the anticipated change in demand over the look-ahead interval. FC2 therefore responds not merely faster to the same demand, but to a different quantity: the demand expected instead of the demand present. FC2's smaller active area would also favour a faster response, and the present results do not separate the contribution of the supervisory scheme from that of the cell geometry.

E. Response to Repeated Load Events

The results presented so far describe a single load event. To establish whether they are characteristic rather than particular to one excursion, D was subjected to the two-cycle variant of the load profile described in Section II, comprising two pulses of identical commanded shape separated by 7 s at baseline load. Fig. 6 compares the two pulses, each aligned to its own start.

The two responses coincide to within the width of the plotted line, and the fine structure that follows the peak recurs in the second pulse at the same amplitude and in the same part of the transient. Divergence is confined to the oscillatory region, where individual peaks fall at slightly different instants relative to the start of each pulse: the oscillation reproduces in frequency and amplitude, but its peaks do not coincide between the two pulses.

The comparison with S is computed from the sampled data over each pulse. The reduction in peak FC1 current and the advantage in propeller power rate are unchanged between the two pulses; the reduction in peak FC1 current rate increases slightly, and the advantage in fuel-cell electrical power rate more substantially, from 14.6% to 26.0%.

The two pulses do not begin from identical conditions: propeller speed recovers to 102.5% of its pre-pulse value in D, so that the second pulse begins at 988 r/min against 963 r/min for the first.

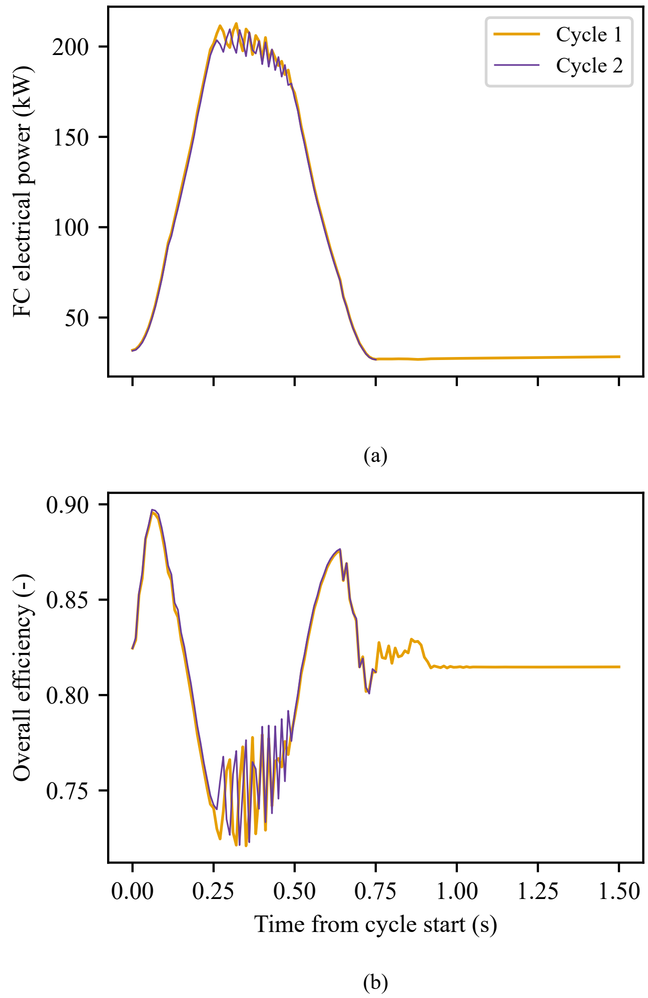

Fig. 6. Comparison of the first and second load pulses for the dual-source configuration, aligned to the start of each pulse. (a) Fuel-cell electrical power. (b) Overall efficiency.

V. Discussion

A. Division of Labour: Magnitude and Timing

Section IV-D reports that FC2 sustains a rate of change of current density approximately 5.7 times that of FC1 for a given excursion in system power. The trajectories in Fig. 5 show that the division between the sources is not limited to the magnitude; timing is also different. FC1's current-density rate lags the fuel-cell power rate, while FC2's leads it, and the two sources traverse their trajectories in opposite senses.

This follows from the structure of the supervisory controller. FC1's allocation is governed principally by the power presently being delivered, so its current follows demand once that demand is established. The variable part of FC2's allocation is governed instead by the anticipated change in demand over the look-ahead interval, so FC2 begins to respond before the demand is realised. The opposite senses of traversal are therefore a signature of the anticipatory mechanism as opposed to a difference in intrinsic response speed.

This is a flexibility that the dual-source configuration affords: the additional source can be tasked with a larger share of the transient, without that task being imposed on the primary source.

Two consequences follow. The two FC1 trajectories, in S and in D, share the same sense of traversal, so introducing FC2 changes the magnitude of FC1's dynamic duty without changing its character; FC1 is relieved not altered. And because FC2 absorbs the anticipated component of the transient, the two sources divide the transient in timing as well as in magnitude, which is a distinction not visible from the peak and cumulative statistics of Table III alone.

B. Where the Differences Between Configurations Reside

Two independent results indicate that the architecture does not alter the electromechanical behaviour downstream of the bus. The correlation between propeller power rate and fuel-cell power rate reported in Section IV-B is close between configurations, as is the propeller speed recovery between pulses reported in Section IV-E. Neither quantity distinguishes the configurations, which indicates that the motor, inverter and propeller respond to the bus in the same manner in both cases, and that what differs is the duty each source carries in supplying it.

The residual oscillation reported in Sections IV-B and IV-E is consistent with the same reading. Its amplitude does not depend on configuration and its character does not depend on repetition, which together point to an origin in the motor, inverter and propeller chain shared by both configurations. This is inferred from the oscillation being the same in both configurations and in both pulses; the present model was not built to trace what physically causes it.

C. Repeatability

The two-cycle results extend the single-cycle findings in a way that a single transient cannot. They show that the fine oscillatory structure is deterministic, since it reproduces in frequency and amplitude on a second, separate pulse.

D. Implications for Battery-Free Operation

The motivation set out in Section I was whether a fuel-cell system might absorb mission transients itself, so that the storage element could be reduced or removed. Neither configuration contains a battery, supercapacitor or other storage device, so the transient capability reported in Section IV is obtained from the fuel-cell system alone. Within that setting, heterogeneity between the sources reduces peak current in the primary fuel-cell source by 36% for a single event, and by 41% across both events of the repeated profile, without raising its current density and while requiring 29% less total active area than the single-source comparator.

The significance of the current-density result is that the relief afforded to FC1 is not obtained at FC1's expense elsewhere. FC1 operates at the same duty per unit of area in both configurations, so the reduction in its current follows from the transient being divided, and not from FC1 being worked harder. FC2 does operate at a higher current density, close to the point of maximum power density for which it is specified, and remains below the limiting current.

The division is also adjustable. Because the share allocated to FC2 is set by the supervisory controller and is not fixed by the hardware, the balance between the two sources can be retuned without altering the fuel cell stacks, which offers a design freedom that a single source does not provide.

These results show that the transient response of a battery-free fuel-cell powertrain can be improved substantially by differentiating the sources, and that the improvement persists across repeated events. A patented aircraft fuel-cell system dispenses with the buffer battery by oversizing the stack and its air compressor, so that the compressor can change speed quickly enough to follow the load, with software smoothing of the demand curve to protect the stack [12]; no performance data for that system have been published. The approach taken here differs in kind. Rather than enlarging a single source, a second source specialised for transient response is added alongside it, and the simulation shows that the two then divide the transient in timing as well as in magnitude. The resulting system requires less membrane area than the single-source comparator, not more.

What these results establish is a precondition, not a demonstration. They do not show that a complete flight mission can be flown without storage, which would require a mission-representative duty cycle and an assessment of thermal and reactant-supply behaviour over far longer timescales than those considered here.

E. Scope and Limitations

The electrochemical parameters underlying every result were calibrated from literature-representative starting points and tuned, not independently validated, as noted in Section II, and the sizing of S inherits the same calibration uncertainty, as noted in Section III. The percentage differences reported in Section IV therefore carry the uncertainty of the calibration, and indicate the size of each effect without fixing its precise value. The qualitative conclusions are less exposed to these sources of uncertainty, since they follow from the structure of the sharing law, level-driven for FC1 and anticipation-driven for FC2, and not from the precise value of any calibrated parameter; a differently tuned model with the same control structure would be expected to show a reduction in FC1 duty and a lead–lag relationship between the sources, even if the specific percentages differed.

Two further limitations in the present study are of scope. The load profile examined here consists of one or two discrete pulses of fixed shape and amplitude; the behaviour of the architecture under a continuous or stochastic duty cycle has not been examined, nor has its sensitivity to the ramp rate or the magnitude of the demanded step. The air path is commanded directly and the dynamics of the air compressor are not represented. And every result is drawn from simulation, with no experimental data available to confirm that the modelled transient response corresponds to that of physical stacks of the sizes considered. This study is accordingly intended to establish whether heterogeneous sizing merits further investigation, and not to characterise the design space it opens.

F. Future Work

The results reported here are drawn from one load profile, one comparator sizing and one control structure, and each of those choices bounds what can be concluded. The extensions below are ordered by what each would add to the present findings.

The sizing of the comparator is the first. Section III-A shows that the equivalence criteria considered give values of $N_{p,\mathrm{S}}$ spanning 7.8 to 11.0, and only the largest is simulated here. Running the comparator at the intermediate sizings would establish whether the transient advantage reported for D survives against a less generously sized single source. A related question is how equal exchange current relates to transient tolerance, since the criterion adopted does not target that property directly.

The second is the load profile. A continuous or stochastic duty cycle representative of a flight, rather than one or two discrete pulses, would test the architecture under the conditions it is intended for, and would allow the sensitivity to ramp rate and to the magnitude of the demanded step to be examined. The transient capability of D is at present bounded by FC2's collapse current rather than by FC1's; raising that bound, by resizing FC2 or by limiting its share of the transient, would extend the range of profiles the architecture can absorb.

The third is the separation of the control law from the hardware. Several of the results reported here follow from how the supervisor allocates load as much as from the presence of two sources, and FC2's smaller active area would act in the same direction as its anticipatory command. Comparing alternative sharing laws on the same hardware, and the same law on sources of differing geometry, would establish how much of the transient behaviour each contributes, and which of the two offers more scope for improvement.

The fourth is model fidelity. The air path is commanded directly, and the dynamics of the air compressor are not represented; where compressor ramp-up limits transient response in hardware, an anticipatory command of the kind already implemented in the supervisor could raise air flow ahead of the demand. Thermal and reactant-supply behaviour over the longer timescales of a complete mission would be required before flight capability could be assessed.

Finally, every result is drawn from simulation with calibrated rather than validated parameters. Experimental confirmation that the modelled transient response corresponds to that of physical stacks of the sizes considered remains the requirement on which the others depend.

VI. Conclusion

This paper has examined whether differentiating the fuel-cell sources of an aircraft powertrain allows mission transients to be met without an energy-storage element. A heterogeneous dual-source configuration was compared against a single-source comparator sized on an explicitly stated equivalence basis, neither containing a battery or supercapacitor.

For a commanded load rise, the dual-source configuration reduced peak current in the primary source by 36% while requiring 29% less total membrane area than the comparator, and delivered higher propeller power at higher efficiency. The current density in the primary source was unchanged, so this relief followed from the way the transient was divided between the two sources and not from the primary source being worked harder. The auxiliary source carried a much higher rate of change of current density than the primary one, and led it in phase, so that the two divided the transient in timing as well as in magnitude. These outcomes were reproduced across a second, separate load event.

The supervisory scheme used here is deliberately simple, and the division between the sources is set by the controller, not fixed by the hardware. Each branch's converter, geometry and coefficient schedule can be specified independently, so the balance between the sources can be retuned without altering either stack.

What these results establish is a precondition for battery-free operation, and not a demonstration of it. On the evidence presented, heterogeneous sizing merits the further investigation set out in Section V-F.

Acknowledgment

The author thanks Dr Tom Fletcher of the Institute for Advanced Automotive Propulsion Systems, University of Bath, for reviewing the manuscript and for detailed comments that shaped several aspects of this work.

References

[1] Airbus, "Airbus and MTU Aero Engines to create a joint venture to develop a fully electric hydrogen fuel cell engine," Press release, Jul. 2026. [Online]. Available: https://www.airbus.com/en/newsroom/press-releases/2026-07-airbus-and-mtu-aero-engines-to-create-a-joint-venture-to-develop-a-fully-electric-hydrogen-fuel-cell

[2] ZeroAvia, "ZA600," Company website. [Online]. Available: https://zeroavia.com/za600/

[3] ——, "ZA2000," Company website. [Online]. Available: https://zeroavia.com/za2000/

[4] S. B. Mousavi, P. Ahmadi, and M. Raeesi, "Performance evaluation of a hybrid hydrogen fuel cell/battery bus with fuel cell degradation and battery aging," *Renewable Energy*, vol. 227, p. 120456, 2024.

[5] T. Graf, R. Fonk, C. Bauer, J. Kallo, and C. Willich, "Optimal sizing of fuel cell and battery in a direct-hybrid for electric aircraft," *Aerospace*, vol. 11, no. 3, p. 176, Feb. 2024.

[6] N. Marx, D. Hissel, F. Gustin, L. Boulon, and K. Agbossou, "On the sizing and energy management of an hybrid multistack fuel cell–battery system for automotive applications," *International Journal of Hydrogen Energy*, vol. 42, pp. 1518–1526, 2017.

[7] S. Zhou, L. Fan, G. Zhang, J. Gao, Y. Lu, P. Zhao *et al.*, "A review on proton exchange membrane multi-stack fuel cell systems: Architecture, performance, and power management," *Applied Energy*, vol. 310, 2022.

[8] D. Liu, Z. Chen, Z. Guo, B. Zhu, G. Jia, and X. Yang, "Analysis of battery weight requirements in the design of hybrid electric powered aircraft," in *Proceedings of the 34th Congress of the International Council of the Aeronautical Sciences (ICAS)*, Florence, Italy, 2024.

[9] T. Pattanayak and D. Mavris, "Battery technology for sustainable aviation: A review of current trends and future prospects," *Applied Energy*, vol. 397, p. 126356, 2025.

[10] J. D. Anderson, *Aircraft Performance and Design*. New York, NY, USA: McGraw-Hill, 1999.

[11] P. A. Hanlon, J. Cashman, Z. Zhong, I. Jakupca, and V. Lvovich, "Modeling and trade space for fuel cell powered aircraft," in *AIAA AVIATION Forum*, Las Vegas, NV, USA, Jul. 2024.

[12] V. Miftakhov, V. Belogorodsky, and I. H. Grishashvili, "Aircraft fuel cell system without the use of a buffer battery," U.S. Patent 11,942,668, Mar. 2024, assignee: ZeroAvia, Inc.

[13] X. Li, K. Han, and Y. Song, "Dynamic behaviors of PEM fuel cells under load changes," *International Journal of Hydrogen Energy*, vol. 45, pp. 20 312–20 320, 2020.

[14] W.-M. Yan, H.-Y. Li, and W.-C. Weng, "Transient mass transport and cell performance of a PEM fuel cell," *International Journal of Heat and Mass Transfer*, vol. 107, pp. 646–656, 2017.

[15] H. Wei, C. Du, F. Ke, J. Zhao, and X. Li, "Air supply management for a 100-kW vehicle fuel cell system with fuzzy self-adaptive anti-disturbance control," *Fuel*, vol. 400, p. 135718, 2025.

[16] M. Seddiq, M. Alnajideen, and R. Navaratne, "Thermal transient performance of PEM fuel cells in aerospace applications: A numerical study," *Energy & Fuels*, vol. 39, no. 16, pp. 7876–7889, 2025.

[17] K. Loo, K. Wong, S. Tan *et al.*, "Characterization of the dynamic response of proton exchange membrane fuel cells: A numerical study," *International Journal of Hydrogen Energy*, vol. 35, no. 21, pp. 11 861–11 877, 2010.

[18] R. Fan, G. Chang, Y. Xu, Y. Zhang, and P. Wei, "Enhancing PEM fuel cell dynamic performance: Co-optimization of cathode catalyst layer composition and operating conditions using a novel surrogate model," *Renewable Energy*, vol. 231, p. 120993, 2024.

[19] P. Liao, D. Yang, X. Pan, B. Li, P. Ming, and Z. Li, "Enhancing dynamic performance of proton exchange membrane fuel cells through two-phase flow experimental investigation," *International Journal of Hydrogen Energy*, vol. 48, pp. 32 093–32 109, 2023.

[20] Y.-B. Kim, "Improving dynamic performance of proton-exchange membrane fuel cell system using time delay control," *Journal of Power Sources*, vol. 195, 2010.

[21] N. Marx, L. Boulon, F. Gustin, D. Hissel, and K. Agbossou, "A review of multi-stack and modular fuel cell systems: Interests, application areas and on-going research activities," *International Journal of Hydrogen Energy*, vol. 39, no. 23, pp. 12 101–12 111, 2014.

[22] L. Palma and P. N. Enjeti, "A modular fuel cell, modular DC-DC converter concept for high performance and enhanced reliability," *IEEE Transactions on Power Electronics*, 2009.

[23] T. N. Ngo and M. Kim, "Efficiency maximization of fuel cell electric bus using asymmetric multi-stack fuel cells," *Heliyon*, vol. 10, no. 19, p. e38286, 2024.

[24] B. Eom, K. Eom, D. Yang *et al.*, "Novel electric vehicle powertrain of multi-stack fuel cell using optimal energy management strategy," *International Journal of Automotive Technology*, vol. 25, pp. 201–211, 2024.

[25] X. Lu, J. M. Guerrero, K. Sun, and J. C. Vasquez, "An improved droop control method for DC microgrids based on low bandwidth communication with DC bus voltage restoration and enhanced current sharing accuracy," *IEEE Transactions on Power Electronics*, vol. 29, no. 4, pp. 1800–1812, 2014.

[26] T. Wang, Q. Li, X. Wang, W. Chen, E. Breaz, and F. Gao, "A power allocation method for multistack PEMFC system considering fuel cell performance consistency," *IEEE Transactions on Industry Applications*, vol. 56, no. 5, pp. 5340–5351, 2020.

[27] Y. Qiu, T. Zeng, C. Zhang *et al.*, "Progress and challenges in multi-stack fuel cell system for high power applications: Architecture and energy management," *Green Energy and Intelligent Transportation*, vol. 2, no. 2, 2023.

[28] A. Datta, "PEM fuel cell model for conceptual design of hydrogen eVTOL aircraft," NASA, Tech. Rep. NASA/CR–20210000284, Jan. 2021.

Mehdi Seddiq received the B.Sc. degree in mechanical engineering from Sharif University of Technology, Tehran, Iran, in 2002, the M.Sc. and Ph.D. degrees in mechanical engineering (fluids and energy conversion) from Tarbiat Modares University, Tehran, Iran, in 2005 and 2012, respectively, and the M.Sc. degree in computational mathematics from Heriot-Watt University, Edinburgh, U.K., in 2018.

He is currently a Research Associate with the School of Science and Technology, City St George's, University of London, London, U.K. He previously held research positions at Cardiff University, working on hybrid electric aircraft powertrains and hydrogen storage systems, and at Swansea University, developing mesh generation software for aerodynamic flows. His doctoral and postdoctoral research has centred on physics-based modelling of electrochemical energy systems, including proton exchange membrane fuel cells and lithium-ion batteries. His current research interests include fuel-cell propulsion for electric aircraft and multiphysics simulation of energy conversion systems.